

# A new determination of the $\eta$ transition form factor in the Dalitz decay $\eta \rightarrow e^+e^-\gamma$ with the Crystal Ball/TAPS detectors at the Mainz Microtron

P. Aguar-Bartolomé<sup>1</sup>, J. R. M. Annand<sup>2</sup>, H. J. Arends<sup>1</sup>, K. Bantawa<sup>3</sup>, R. Beck<sup>4</sup>, V. Bekrenev<sup>5</sup>, H. Berghäuser<sup>6</sup>, A. Braghieri<sup>7</sup>, W. J. Briscoe<sup>8</sup>, J. Brudvik<sup>9</sup>, S. Cherepnya<sup>10</sup>, R. F. B. Codling<sup>2</sup>, C. Collicott<sup>11,12</sup>, S. Costanza<sup>7</sup>, A. Denig<sup>1</sup>, E. J. Downie<sup>1,8</sup>, P. Drexler<sup>6</sup>, L. V. Fil'kov<sup>10</sup>, A. Fix<sup>13</sup>, D. I. Glazier<sup>14</sup>, R. Gregor<sup>6</sup>, D. J. Hamilton<sup>2</sup>, E. Heid<sup>1,8</sup>, D. Hornidge<sup>15</sup>, L. Isaksson<sup>16</sup>, I. Jaegle<sup>17</sup>, O. Jahn<sup>1</sup>, T. C. Jude<sup>14</sup>, V. L. Kashevarov<sup>1,10</sup>, I. Keshelashvili<sup>17</sup>, R. Kondratiev<sup>18</sup>, M. Korolija<sup>19</sup>, M. Kotulla<sup>6</sup>, A. Koulbardi<sup>5</sup>, S. Kruglov<sup>5</sup>, B. Krusche<sup>17</sup>, V. Lisin<sup>18</sup>, K. Livingston<sup>2</sup>, I. J. D. MacGregor<sup>2</sup>, Y. Maghrbi<sup>17</sup>, D. M. Manley<sup>3</sup>, P. Masjuan<sup>1</sup>, J. C. McGeorge<sup>2</sup>, E. F. McNicoll<sup>2</sup>, D. Mekterovic<sup>19</sup>, V. Metag<sup>6</sup>, A. Mushkarenkov<sup>7</sup>, B. M. K. Nefkens<sup>9</sup>, A. Nikolaev<sup>4</sup>, R. Novotny<sup>6</sup>, H. Ortega<sup>1</sup>, M. Ostrick<sup>1</sup>, P. Ott<sup>1</sup>, P. B. Otte<sup>1</sup>, B. Oussena<sup>1,8</sup>, P. Pedroni<sup>7</sup>, F. Pheron<sup>17</sup>, A. Polonski<sup>18</sup>, S. Prakhov<sup>1,8,9\*</sup>, J. Robinson<sup>2</sup>, G. Rosner<sup>2</sup>, T. Rostomyan<sup>17</sup>, S. Schumann<sup>1</sup>, M. H. Sikora<sup>14</sup>, D. I. Sober<sup>20</sup>, A. Starostin<sup>9</sup>, I. I. Strakovsky<sup>8</sup>, I. M. Suarez<sup>9</sup>, I. Supek<sup>19</sup>, C. M. Tarbert<sup>14</sup>, M. Thiel<sup>6</sup>, A. Thomas<sup>1</sup>, M. Unverzagt<sup>1,4†</sup>, D. P. Watts<sup>14</sup>, D. Werthmüller<sup>17</sup>, and F. Zehr<sup>17</sup>

(A2 Collaboration at MAMI)

<sup>1</sup>*Institut für Kernphysik, University of Mainz, D-55099 Mainz, Germany*

<sup>2</sup>*Department of Physics and Astronomy, University of Glasgow, Glasgow G12 8QQ, United Kingdom*

<sup>3</sup>*Kent State University, Kent, Ohio 44242-0001, USA*

<sup>4</sup>*Helmholtz-Institut für Strahlen- und Kernphysik, University of Bonn, D-53115 Bonn, Germany*

<sup>5</sup>*Petersburg Nuclear Physics Institute, 188350 Gatchina, Russia*

<sup>6</sup>*II Physikalisches Institut, University of Giessen, D-35392 Giessen, Germany*

<sup>7</sup>*INFN Sezione di Pavia, I-27100 Pavia, Italy*

<sup>8</sup>*The George Washington University, Washington, DC 20052-0001, USA*

<sup>9</sup>*University of California Los Angeles, Los Angeles, California 90095-1547, USA*

<sup>10</sup>*Lebedev Physical Institute, 119991 Moscow, Russia*

<sup>11</sup>*Dalhousie University, Halifax, Nova Scotia B3H 4R2, Canada*

<sup>12</sup>*Saint Mary's University, Halifax, Nova Scotia B3H 3C3, Canada*

<sup>13</sup>*Laboratory of Mathematical Physics, Tomsk Polytechnic University, 634050 Tomsk, Russia*

<sup>14</sup>*School of Physics, University of Edinburgh, Edinburgh EH9 3JZ, United Kingdom*

<sup>15</sup>*Mount Allison University, Sackville, New Brunswick E4L 1E6, Canada*

<sup>16</sup>*Lund University, SE-22100 Lund, Sweden*

<sup>17</sup>*Institut für Physik, University of Basel, CH-4056 Basel, Switzerland*

<sup>18</sup>*Institute for Nuclear Research, 125047 Moscow, Russia*

<sup>19</sup>*Rudjer Boskovic Institute, HR-10000 Zagreb, Croatia and*

<sup>20</sup>*The Catholic University of America, Washington, DC 20064, USA*

(Dated: June 25, 2018)

The Dalitz decay  $\eta \rightarrow e^+e^-\gamma$  has been measured in the  $\gamma p \rightarrow \eta p$  reaction with the Crystal Ball and TAPS multiphoton spectrometers, together with the photon tagging facility at the Mainz Microtron MAMI. The experimental statistic used in this work is one order of magnitude greater than in any previous measurement of  $\eta \rightarrow e^+e^-\gamma$ . The value obtained for the slope parameter  $\Lambda^{-2}$  of the  $\eta$  transition form factor,  $\Lambda^{-2} = (1.95 \pm 0.15_{\text{stat}} \pm 0.10_{\text{syst}}) \text{ GeV}^{-2}$ , is in good agreement with recent measurements conducted in  $\eta \rightarrow e^+e^-\gamma$  and  $\eta \rightarrow \mu^+\mu^-\gamma$  decays, as well as with recent form-factor calculations. The uncertainty obtained in the value of  $\Lambda^{-2}$  is lower compared to results from previous measurements of the  $\eta \rightarrow e^+e^-\gamma$  decay.

PACS numbers: 14.40.Be, 13.20.-v, 13.40.Gp

## I. INTRODUCTION

The determination of electromagnetic transition form factors (TFFs) of light pseudoscalar mesons  $P$  is of crucial importance for understanding the intrinsic structure

of these particles (see Ref. [1] and references therein). A special role is occupied by the  $P \rightarrow \gamma^*\gamma \rightarrow e^+e^-\gamma$  decays of light neutral mesons [2]. As this decay includes only one hadron, the TFF fully describes the electromagnetic structure of the particle. For structureless mesons, the decay rate can be calculated within Quantum Electrodynamics (QED). The complex internal structure of mesons incorporated in the TFF modifies the decay rate. By measuring the decay rate and dividing it by the QED contribution, the TFF can be determined.

\*corresponding author; e-mail: prakhov@ucla.edu

†corresponding author; e-mail: unvemarc@kph.uni-mainz.de

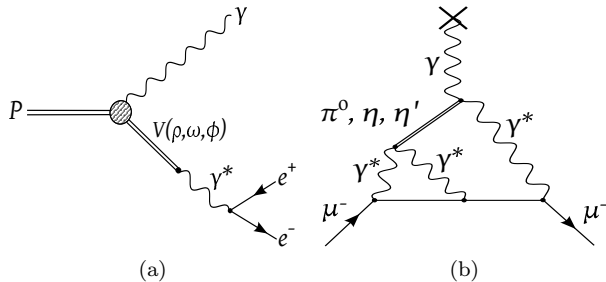


FIG. 1: Feynman diagrams illustrating (a) the  $P \rightarrow \gamma^*\gamma$  transition in VMD and (b) one of the leading contributions to the correction for  $(g-2)_\mu$  due to the hadronic light-by-light scattering.

Decays of light pseudoscalar mesons ( $\pi^0$ ,  $\eta$ , and  $\eta'$ ) into a real and a virtual photon are ideally suited for testing the Vector Meson Dominance (VMD) model [3]. In VMD, the coupling of a virtual photon to a pseudoscalar meson is described via an intermediate virtual vector meson  $V$  (see Fig. 1(a)). This mechanism is especially strong in the timelike momentum-transfer region, where a resonancelike behavior near momentum transfer  $q^2 = m_V^2$  of the virtual photon arises because the virtual vector meson reaches the mass shell [2].

The TFFs of the  $\eta$  and  $\eta'$  mesons are strongly related to the mixing of these particles [4]. With quarks as inner degrees of freedom in Quantum Chromodynamics (QCD), several symmetry-breaking mechanisms (U(1) axial anomaly and dynamical and explicit chiral-symmetry breaking) lead to a mixing of the pure SU(3) states  $|\eta_q\rangle = \frac{1}{\sqrt{2}}|u\bar{u} + d\bar{d}\rangle$  and  $|\eta_s\rangle = |s\bar{s}\rangle$  in the quark-flavor basis to form the  $\eta$  and  $\eta'$  mesons. In the picture of VMD, the coupling of light vector-meson resonances ( $\omega$ ,  $\rho$ , and  $\phi$ ) to the virtual photon influences the slope of the TFF. Since the  $\phi$  meson is a pure  $s\bar{s}$  state, measuring the TFF precisely gives stringent constraints on the strange-quark content of the  $\eta$  and  $\eta'$  mesons [2]. In addition, a possible gluonic contribution to  $\eta$  and  $\eta'$  is currently under discussion [5], which could be investigated with TFFs. If such an effect existed, it would have to be included in  $\eta$ - $\eta'$  mixing schemes. Exploring the TFFs of the  $\eta$  and  $\eta'$  mesons sheds new light not only on the quark structure of these particles but also on the interplay of the symmetry-breaking mechanisms that were mentioned above.

It has been argued [6] that TFFs might be related to the contribution of the hadronic light-by-light scattering to the anomalous magnetic moment of the muon,  $(g-2)_\mu$ , which is one of the limiting contributions for the Standard Model (SM) calculation of this precision observable. Since the contribution of the hadronic light-by-light scattering can not be accessed directly through experiments, models describing  $P\gamma^*\gamma$  transitions are needed to calculate this contribution. A diagram showing one of the leading contributions to the correction due to the hadronic light-by-light scattering is depicted in Fig. 1(b).

Here two vertices appear where pseudoscalar mesons couple to virtual photons and the external magnetic field. Experiments can measure such vertices in other processes, e.g., decays of pseudoscalar mesons, and this way act as a testing ground for VMD or VMD-based models describing  $P\gamma^*\gamma$  transitions (see Ref. [6] and references therein) and provide appropriate input parameters for these models. Thus, the models describing the  $P\gamma^*\gamma$  transitions have to be tested as precisely as possible to reduce the uncertainty in the SM prediction for  $(g-2)_\mu$ . Calculations of the contribution from the hadronic light-by-light scattering to  $(g-2)_\mu$  are performed in the spacelike momentum-transfer region, although it is also possible to do in the timelike regime. The dominant energy region for such calculations turns out to be the low-energy region up to  $1 \text{ GeV}^2$ , exactly where the slope of the TFF is the relevant parameter. Since the TFF is continuous at  $q^2 = 0 \text{ GeV}^2$ , this value can be determined in both the momentum regions. It is currently not possible to reach the lowest  $q^2$  values experimentally in the spacelike regime. On the contrary, determining TFFs with high precision is possible from Dalitz decays. Thus, measurements of the timelike TFF with Dalitz decays are important for fixing the slope at  $q^2 = 0 \text{ GeV}^2$ , especially by studying decays like  $\eta \rightarrow l^+l^-\gamma$  with the  $e^+e^-$  lepton pair, making it possible to reach a much lower value of  $q^2 = 4m_l^2$  than with  $\mu^+\mu^-$ .

Experimentally, TFFs can be explored through different techniques in three separate momentum-transfer regions. The spacelike region,  $q^2 < 0 \text{ GeV}^2$ , can be studied at an  $e^+e^-$  collider via the  $\gamma^*\gamma \rightarrow P$  process in the  $e^+e^- \rightarrow e^+e^-P$  reaction (see Fig. 2(a)). The lowest timelike  $q^2$  region,  $(2m_l)^2 < q^2 < m_P^2$ , is accessible only through studying meson decays, where  $2m_l$  is the mass of the two leptons from the virtual-photon decay (see Fig. 2(b)). Above  $q^2 = m_P^2$ , TFFs can be investigated in  $e^+e^-$ -annihilation processes,  $e^+e^- \rightarrow P\gamma$  (Fig. 2(c)), at collider experiments.

In this work, a new determination of the timelike  $\eta$  TFF in the low- $q^2$  region is presented. Experimentally, such a determination can be done by measuring the decay rate of  $\eta \rightarrow \gamma^*\gamma \rightarrow l^+l^-\gamma$  as a function of a dilepton invariant mass  $m_{ll} = q$  and normalizing it to the partial decay width  $\Gamma(\eta \rightarrow \gamma\gamma)$  [2]:

$$\begin{aligned} \frac{d\Gamma(\eta \rightarrow l^+l^-\gamma)}{dm_{ll}\Gamma(\eta \rightarrow \gamma\gamma)} &= \\ &= \frac{4\alpha}{3\pi m_{ll}} \left[1 - \frac{4m_l^2}{m_{ll}^2}\right]^{\frac{1}{2}} \cdot \left[1 + \frac{2m_l^2}{m_{ll}^2}\right] \cdot \left[1 - \frac{m_{ll}^2}{m_\eta^2}\right]^3 \cdot |F_\eta(m_{ll})|^2 \\ &= [QED] \cdot |F_\eta(m_{ll})|^2, \end{aligned} \quad (1)$$

where  $F_\eta$  is the TFF of the  $\eta$  meson and  $m_\eta$  is the mass of the  $\eta$  meson. Assuming VMD, transition form factors are usually parametrized as

$$F(m_{ll}) = \frac{1}{1 - \frac{m_{ll}^2}{\Lambda^2}}, \quad (2)$$

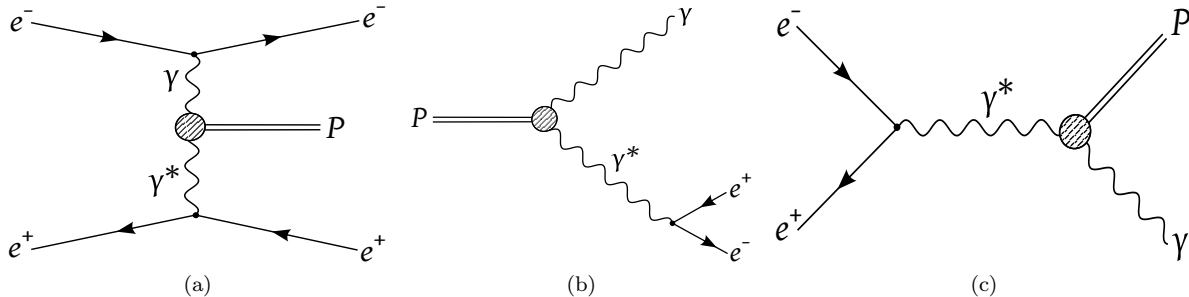


FIG. 2: Feynman diagrams showing the processes with the  $P \rightarrow \gamma^* \gamma$  transition that can be used for investigating TFFs of light pseudoscalar mesons  $P$  in three different  $q^2$  regions: (a) spacelike ( $q^2 < 0 \text{ GeV}^2$ ), (b) timelike ( $(2m_l)^2 < q^2 < m_P^2$ ), and (c) timelike ( $q^2 > m_P^2$ ).

where  $\Lambda$  is the effective mass of the virtual vector mesons. The parameter  $b = \Lambda^{-2}$  reflects the form-factor slope at  $m_{ll} = 0$ . A simple VMD model would incorporate only the  $\rho$ ,  $\omega$ , and  $\phi$  resonances (in the narrow-width approximation) as virtual vector mesons driving a photon interaction with a pseudoscalar. Using a quark model to account for the corresponding couplings would yield the TFF slope  $b = 1.8 \text{ GeV}^{-2}$  [2], corresponding to  $\Lambda = 745 \text{ MeV}$ .

So far, the most precise measurement of the parameter  $\Lambda^{-2}$  in the Dalitz decay  $\eta \rightarrow e^+ e^- \gamma$  was reported in 2011 by the A2 Collaboration at MAMI [7]. The value obtained,  $\Lambda^{-2} = (1.92 \pm 0.35_{\text{stat}} \pm 0.13_{\text{syst}}) \text{ GeV}^{-2}$ , is based on an analysis of  $1.35 \cdot 10^3$   $\eta \rightarrow e^+ e^- \gamma$  decays. At the same time, an analysis of the  $\eta \rightarrow \mu^+ \mu^- \gamma$  decay by the NA60 Collaboration allowed a determination of  $\Lambda^{-2}$  with significantly better statistical accuracy. In 2009, the NA60 Collaboration reported the value  $\Lambda^{-2} = (1.95 \pm 0.17_{\text{stat}} \pm 0.05_{\text{syst}}) \text{ GeV}^{-2}$  based on an analysis of  $9 \cdot 10^3$   $\eta \rightarrow \mu^+ \mu^- \gamma$  decays in peripheral In-In data [8]. Recently, NA60 presented an improved preliminary result,  $\Lambda^{-2} = (1.951 \pm 0.059_{\text{stat}} \pm 0.042_{\text{syst}}) \text{ GeV}^{-2}$ , based on an analysis of  $8 \cdot 10^4$  low-mass muon pairs produced in  $p - A$  collisions [9].

The major shortcoming of using the  $\eta \rightarrow \mu^+ \mu^- \gamma$  Dalitz decay for the determination of the  $\eta$  TFF is the inability to measure  $d\Gamma(\eta \rightarrow l^+ l^- \gamma)/dm_{ll}$  below  $m_{ll} = 2m_\mu$ . This limitation does not allow a check of whether the experimental points approach  $F_\eta = 1$  at  $m_{ll} = 0$ , as it was assumed in their final fit. Besides, the measurement of the NA60 Collaboration is based on fitting all possible contributions to the entire spectrum of the  $\mu^+ \mu^-$  invariant masses, without detecting the final-state photon and reconstructing the  $\eta$  meson from its decay products.

Using the  $\eta \rightarrow e^+ e^- \gamma$  Dalitz decay for the determination of the  $\eta$  TFF allows for measuring  $d\Gamma(\eta \rightarrow l^+ l^- \gamma)/dm_{ll}$  much closer to  $m_{ll} = 0$  and to fit a function with two free parameters to the data points. One of the function parameters is  $\Lambda^{-2}$  itself; the other reflects the uncertainty in the general normalization of the data points. Such uncertainty could emerge, for example, from the experimental determination of the number of  $\eta$  mesons produced, which is needed for calculating

$d\Gamma(\eta \rightarrow l^+ l^- \gamma)/dm_{ll}$ .

The results of the work presented in this paper are based on an analysis of  $2.2 \cdot 10^4$   $\eta \rightarrow e^+ e^- \gamma$  decays from a total of  $3 \cdot 10^7$   $\eta$  mesons produced in the  $\gamma p \rightarrow \eta p$  reaction. About one-third of these data have already been used in the previous analysis by the A2 Collaboration at MAMI [7]. Compared to the analysis of Ref. [7], further increase in statistic was also achieved through exploiting the full production energy range for  $\eta$  mesons, using, unlike the former analysis, a kinematic-fit technique for event identification, and substantially revising the criteria used for event selection.

## II. EXPERIMENTAL SETUP

The process  $\gamma p \rightarrow \eta p \rightarrow e^+ e^- \gamma p$  was measured using the Crystal Ball (CB) [10] as the central spectrometer and TAPS [11, 12] as a forward spectrometer. These detectors were installed in the energy-tagged bremsstrahlung photon beam of the Mainz Microtron (MAMI) [13, 14]. The photon energies were determined by the Glasgow-Mainz tagging spectrometer [15–17].

The CB detector is a sphere consisting of 672 optically isolated NaI(Tl) crystals, shaped as truncated triangular pyramids, which point toward the center of the sphere. The crystals are arranged in two hemispheres that cover 93% of  $4\pi$  sr, sitting outside a central spherical cavity with a radius of 25 cm, which is designed to hold the target and inner detectors. In this experiment, TAPS was arranged in a plane consisting of 384 BaF<sub>2</sub> counters of hexagonal cross section. It was installed 1.5 m downstream of the CB center and covered the full azimuthal range for polar angles from  $1^\circ$  to  $20^\circ$ .

The present analysis is based on the same data set that was used to study the  $\eta \rightarrow 3\pi^0$  decay [18] and to measure the  $\gamma p \rightarrow \eta p$  differential cross sections [19]. The experiment was conducted in 2007 by using the 1508-MeV electron beam from the Mainz Microtron, MAMI-C [14]. Bremsstrahlung photons, produced by the 1508-MeV electrons in a  $10\text{-}\mu\text{m}$  Cu radiator and collimated by a 4-mm-diameter Pb collimator, were incident on a 5-cm-long liquid hydrogen (LH<sub>2</sub>) target located in the center

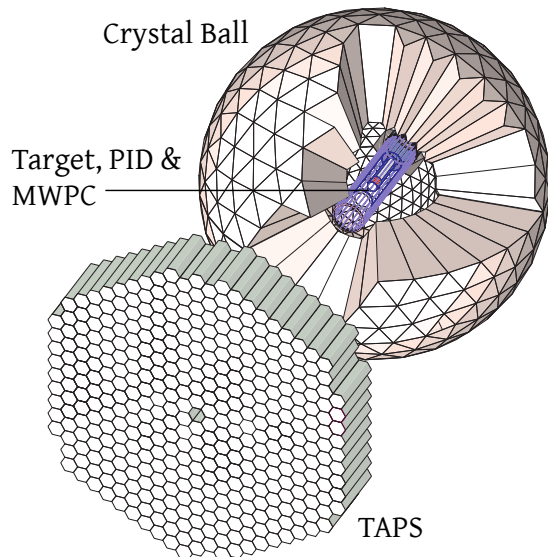


FIG. 3: (Color online) A general sketch of the CB, TAPS, and PID detectors.

of the CB. The total amount of the material around the target, including the Kapton cell and the 1-mm-thick carbonfiber beamline, was equivalent to 0.8% of a radiation length  $X_0$ . In the present measurement, it was essential to keep the material budget as low as possible to diminish the  $\eta \rightarrow \gamma\gamma$  background with conversion of real photons into  $e^+e^-$  pairs.

The energies of the incident photons were analyzed up to 1402 MeV by detecting the postbremsstrahlung electrons in the Glasgow-Mainz tagger [15]. The energy resolution of the tagged photons is mostly defined by the width of the tagger focal-plane detectors and by the electron-beam energy. For the present beam energies, a typical width of a tagger channel was about 4 MeV.

The target was surrounded by a Particle IDentification (PID) detector [20] used to distinguish between charged and neutral particles. It was made of 24 scintillator bars (50 cm long, 4 mm thick) arranged as a cylinder with a radius of 12 cm.

The experimental data were taken with a trigger that required, first, the total-energy deposit in the CB to exceed  $\sim 320$  MeV and, second, the number of so-called hardware clusters in the CB (multiplicity trigger) to be larger than two. Depending on the data-taking period, events with cluster multiplicity two were prescaled with a different rate. TAPS was not in the multiplicity trigger for these experiments.

More details on the experimental resolutions of the detectors and other conditions during these measurements are given in Refs. [18, 19]. A general sketch of the CB, TAPS, and PID is shown in Fig. 3.

### III. DATA HANDLING

Candidates for the process  $\gamma p \rightarrow \eta p \rightarrow e^+e^-\gamma p$  were extracted from the analysis of events having three and four clusters reconstructed in the CB and TAPS together. The three-cluster events were analyzed assuming that the final-state proton was not detected. The selection of event candidates was based on the kinematic-fit technique. The details of the kinematic-fit parametrization of the detector information and resolution are given in Ref. [18]. Since electromagnetic ( $e/m$ ) showers from electrons and positrons are very similar to those of photons, the hypothesis  $\gamma p \rightarrow 3\gamma p$  was tested to identify the  $\gamma p \rightarrow e^+e^-\gamma p$  candidates. The events that satisfied this hypothesis with a probability greater than 2% were accepted as possible reaction candidates. The kinematic-fit output was used to reconstruct the reaction kinematics. In this output, there was no identification of which  $e/m$  shower belonged to the outgoing photon, electron, or positron. Since the main purpose of the experiment was to measure the  $\eta \rightarrow e^+e^-\gamma$  decay rate as a function of the invariant mass  $m(e^+e^-)$ , the next step of the analysis was to separate the final-state photon from the electron and positron. This procedure was optimized by using a Monte Carlo (MC) simulation of the process  $\gamma p \rightarrow \eta p \rightarrow e^+e^-\gamma p$ .

To reproduce the experimental yield of the  $\eta \rightarrow e^+e^-\gamma$  decays depending on the incident-photon energy, the  $\gamma p \rightarrow \eta p$  reaction was generated according to its excitation function, measured in the same experiment [19], which was then folded with the bremsstrahlung energy dependence of the incident photons. Since the energy range used in the analysis covers almost 700 MeV of the photon beam energies, the production angular distribution of  $\gamma p \rightarrow \eta p$  changes with energy. As this distribution averaged over all energies is sufficiently close to an isotropic distribution, for simplicity, the production angle was generated isotropically. The  $\eta \rightarrow e^+e^-\gamma$  decay was generated according to Eq. (1), assuming the  $\eta$  transition form factor  $F_\eta = 1$ .

Possible background processes were studied via MC simulation. The reaction  $\gamma p \rightarrow \eta p$  was simulated for several other decay modes of the  $\eta$  meson to check if they could mimic a peak from the  $\eta \rightarrow e^+e^-\gamma$  signal. Such MC simulations were made for the  $\eta \rightarrow \gamma\gamma$ ,  $\eta \rightarrow \pi^0\pi^0\pi^0$ ,  $\eta \rightarrow \pi^+\pi^-\pi^0$ , and  $\eta \rightarrow \pi^+\pi^-\gamma$  decays. The energy dependence and the production angular distribution of all  $\gamma p \rightarrow \eta p$  simulations were generated in the same way as for the process  $\gamma p \rightarrow \eta p \rightarrow e^+e^-\gamma p$ . In contrast to the  $\eta \rightarrow e^+e^-\gamma$  decay, all other decays of  $\eta$  were generated according to phase space.

The major background under the peak from  $\eta \rightarrow e^+e^-\gamma$  decays was found to be from the reaction  $\gamma p \rightarrow \pi^0\pi^0 p$ . The MC simulation of this reaction was done in the same way as reported in Ref. [21]. Although this background is smooth in the region of the  $\eta$  mass and cannot mimic an  $\eta \rightarrow e^+e^-\gamma$  peak, its MC simulation was used for optimizing the signal-to-background ratio

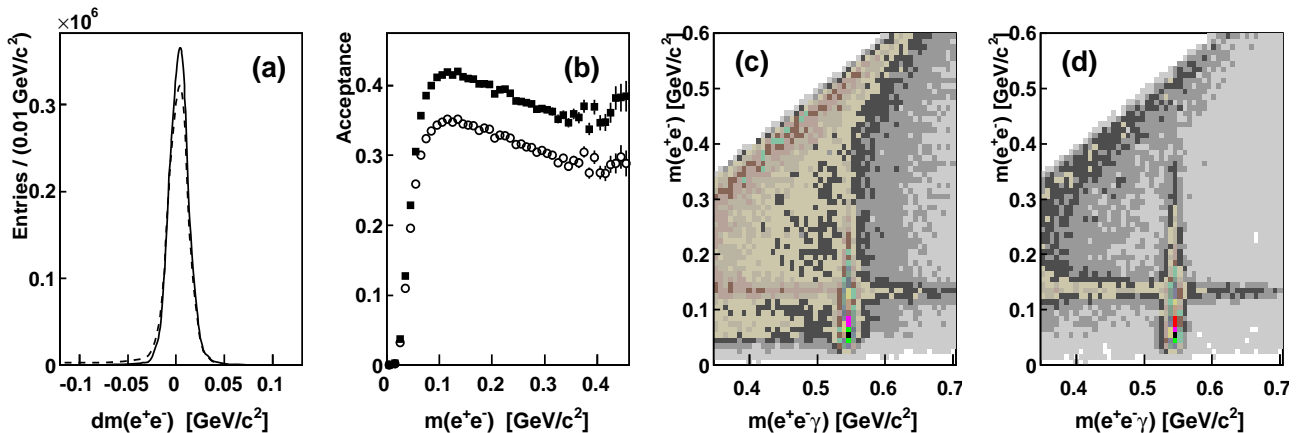


FIG. 4: (Color online) (a) Difference between the generated and reconstructed invariant mass  $m(e^+e^-)$  for the MC simulation of  $\gamma p \rightarrow \eta p \rightarrow e^+e^- \gamma p$  shown for three- (dashed line) and four-cluster (solid line) events, where both the distributions are normalized to each other; (b) The  $\gamma p \rightarrow \eta p \rightarrow e^+e^- \gamma p$  acceptance as a function of  $m(e^+e^-)$  shown for all (solid squares) and for only four-cluster (open circles) events; (c) and (d) Distributions of the invariant mass  $m(e^+e^-)$  as a function of the invariant mass  $m(e^+e^- \gamma)$  for the experimental  $\gamma p \rightarrow e^+e^- \gamma p$  candidates shown for all and only four-cluster events, respectively.

and parametrizing the background under the signal.

For all reactions, the simulated events were propagated through a GEANT (version 3.21) simulation of the experimental setup. To reproduce resolutions of the experimental data, the GEANT output (energy and timing) was subject to additional smearing, thus allowing both the simulated and experimental data to be analyzed in the same way. The simulated events were also tested to check whether they passed the trigger requirements.

The optimization of other selection cuts was based on the analysis of the  $\eta \rightarrow e^+e^- \gamma$  candidates selected with the kinematic fit to the experimental data and MC simulations. As it turned out, the  $\gamma p \rightarrow e^+e^- \gamma p$  decays in the three-cluster sample (i.e., without the outgoing proton detected) have a level of background under the peak from  $\eta \rightarrow e^+e^- \gamma$  that is significantly larger than in the four-cluster sample. This background was partially suppressed by testing the kinematic-fit hypotheses  $\gamma p \rightarrow \pi^0 p \rightarrow \gamma \gamma p$  and  $\gamma p \rightarrow \eta p \rightarrow \gamma \gamma p$  to the same events, then rejecting those for which the probability to be  $\gamma p \rightarrow \pi^0 p$  or  $\gamma p \rightarrow \eta p$  was greater than  $10^{-6}$  and  $10^{-5}$ , respectively.

The PID detector was used to separate both the final-state electron and positron (the detection efficiency for  $e^{+(-)}$  in the PID is close to 100%) from the outgoing photon. Since, with respect to the target, the PID provides a full coverage only for the CB crystals, events with only three  $e/m$  showers in the CB were selected for further analysis. Besides improving significantly the separation of electrons and positrons from photons with the PID, this criterion makes almost all selected events pass the trigger requirements (the total energy and the multiplicity in the CB). The identification of electrons and positrons was based on a correlation between the  $\phi$  angles of fired PID elements with the angles of  $e/m$  showers in the CB. The MC simulation of  $\gamma p \rightarrow \eta p \rightarrow e^+e^- \gamma p$  was

used to optimize this procedure, minimizing a probability of misidentification of the photon with either the electron or the positron. Such misidentification can occur, for example, if the  $\phi$  angle of the photon is close to the angle of the electron or the positron. The efficiency of the identification procedure was tested by comparing the generated invariant mass  $m(e^+e^-)$  with the reconstructed invariant mass. In Fig. 4(a), the difference between the generated and reconstructed  $m(e^+e^-)$  values are shown for both three- (dashed line) and four-cluster (solid line) events. As seen, the  $m(e^+e^-)$  invariant-mass resolution, determined by the kinematic-fit technique, is slightly better for the four-cluster events,  $\sigma_m = 9.7 \text{ MeV}/c^2$ , compared to  $\sigma_m = 10.3 \text{ MeV}/c^2$  for the three-cluster events. This is caused by using the outgoing-proton information in the kinematic fit. Misidentification of the outgoing photon with either the electron or the positron is very small. As found from the MC simulation of  $\gamma p \rightarrow \eta p \rightarrow e^+e^- \gamma p$ , this misidentification typically occurs for high  $m(\gamma e^{+(-)})$  masses ( $> 0.46 \text{ GeV}/c^2$ ), which correspond to highly populated low  $m(e^+e^-)$  masses. However, the analysis of the experimental data showed that this misidentification is not crucial for measuring the  $\eta p \rightarrow e^+e^- \gamma p$  signal, as it cannot be determined at  $m(e^+e^-) > 0.46 \text{ GeV}/c^2$  because of a too low signal-to-background ratio.

The analysis of the MC simulations for all background reactions revealed that only the process  $\gamma p \rightarrow \eta p \rightarrow \gamma \gamma p$  could mimic the  $\eta \rightarrow e^+e^- \gamma$  peak. This can occur mostly when one of the final-state photons converts into an electron-positron pair in the material between the production vertex and the NaI(Tl) surface, or when the photon shower inside the CB splits into two energetic subshowers, reconstructed then as two separate clusters (so-called cluster split-offs). This background was partially suppressed by optimizing the cluster algorithm and by requiring the number of the fired PID elements to be

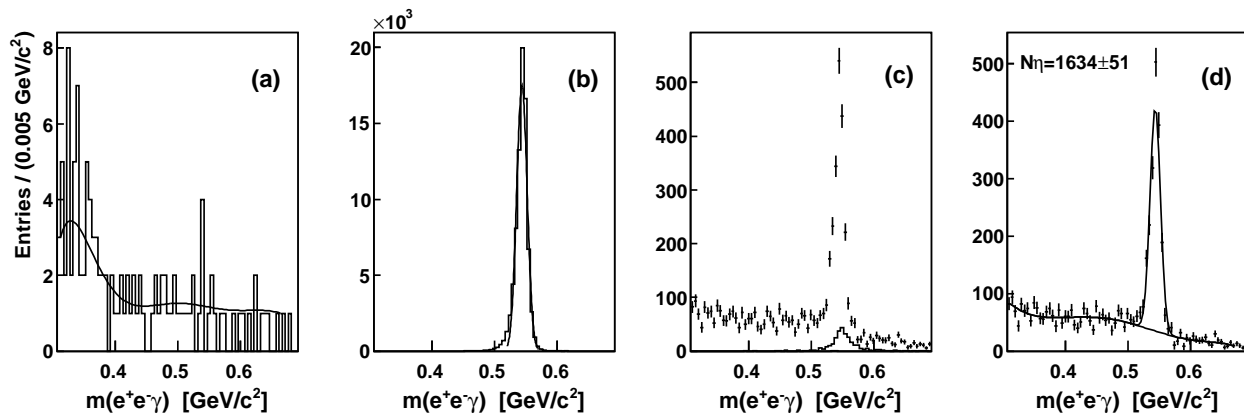


FIG. 5:  $m(e^+e^- \gamma)$  invariant-mass distributions obtained for  $m(e^+e^-) = (45 \pm 5) \text{ MeV}/c^2$  by using both the three- and the four-cluster events: (a) MC simulation of the background reaction  $\gamma p \rightarrow \pi^0 \pi^0 p$  with a polynomial fit; (b) MC simulation of  $\gamma p \rightarrow \eta p \rightarrow e^+e^- \gamma p$  with a Gaussian fit; (c) experimental events (crosses) after subtracting the random and empty-target background; background expected from  $\gamma p \rightarrow \eta p \rightarrow \gamma \gamma p$  (solid line); (d) experimental events from (c) after subtracting the  $\gamma p \rightarrow \eta p \rightarrow \gamma \gamma p$  background fitted with the sum of a Gaussian and a polynomial.

greater than one. The loss of good  $\eta \rightarrow e^+e^- \gamma$  events because of the PID cut is small, as it corresponds to a case when the electron and positron have very close  $\phi$  angles.

Besides the so-called physical background, there are two more background sources. The first one comes from interactions of incident photons in the windows of the target cell. The subtraction of this background from experimental spectra was based on an analysis of data samples that were taken with an empty (no liquid hydrogen) target. Another background is due to random coincidences of the tagger hits with the experimental trigger; its subtraction was done by using only those tagger hits for which all coincidences were random (see Refs. [18, 19] for more details).

In Fig. 4(b), the resulting  $\gamma p \rightarrow \eta p \rightarrow e^+e^- \gamma p$  acceptance is shown as a function of the invariant mass  $m(e^+e^-)$  for two cases: sum of three- and four-cluster events (solid squares) and four-cluster events only (open circles). The  $m(e^+e^-)$  acceptance reached for the four-cluster events in the present work is about five times better than the acceptance reported in Ref. [7]. Including the three-cluster events in the analysis gains an additional 20% in the acceptance. The acceptance shown in Fig. 4(b) is calculated as a ratio of the reconstructed events that passed all selection criteria to the all events generated for  $\gamma p \rightarrow \eta p \rightarrow e^+e^- \gamma p$ . Since the  $\eta \rightarrow e^+e^- \gamma$  decay was generated according to Eq. (1), the number of generated events with large  $m(e^+e^-)$  masses is much smaller than those with low  $m(e^+e^-)$ . The increase seen in the  $m(e^+e^-)$  acceptance above  $0.4 \text{ GeV}/c^2$  is artificial; it occurs owing to a self-background from the events that have large  $m(\gamma e^{+(-)})$  masses and the outgoing photon is misidentified with the electron or the positron. As for the generated  $\eta \rightarrow e^+e^- \gamma$  decays, large  $m(\gamma e^{+(-)})$  masses correspond to the highly populated region of low  $m(e^+e^-)$  masses, the amount of the self-background

events reconstructed with large  $m(e^+e^-)$  masses is comparable with the number of the actual events at this  $m(e^+e^-)$  range. Those self-background events are typically spread wider in the  $m(e^+e^- \gamma)$  distribution and can be partially eliminated by reevaluating the acceptance with a Gaussian fit to the peak from  $\eta \rightarrow e^+e^- \gamma$  decays (how it was done in the fitting procedure described later).

The level of background, remaining under the  $\eta \rightarrow e^+e^- \gamma$  signal in the experimental  $\gamma p \rightarrow e^+e^- \gamma p$  candidates for different invariant masses  $m(e^+e^-)$ , can be seen in Figs. 4(c) and 4(d), in which the invariant mass  $m(e^+e^-)$  is shown as a function of the invariant mass  $m(e^+e^- \gamma)$  for all and only the four-cluster events, respectively. As seen, despite a lower acceptance, the four-cluster events have much smaller background under the  $\eta \rightarrow e^+e^- \gamma$  signal. This becomes especially crucial for observing the signal at higher invariant masses  $m(e^+e^-)$ . Another relatively large background is accumulated in the region of  $m(e^+e^-)$  masses close to the  $\pi^0$  mass, which is seen in Figs. 4(c) and 4(d) as a horizontal band. According to the analysis of the MC simulations for background reactions, this band is caused by the  $\gamma p \rightarrow \pi^0 \pi^0 p$  background.

To measure the  $\eta \rightarrow e^+e^- \gamma$  yield as a function of the invariant mass  $m(e^+e^-)$ , the data were divided into several bins along  $m(e^+e^-)$ . Then the peak from the  $\eta \rightarrow e^+e^- \gamma$  decays was fitted individually in every  $m(e^+e^-)$  bin for two cases: using all  $\gamma p \rightarrow e^+e^- \gamma p$  candidates and the four-cluster events only. The width of the  $m(e^+e^-)$  bins was  $10 \text{ MeV}/c^2$  for  $m(e^+e^-) < 100 \text{ MeV}/c^2$ , where the acceptance drops rapidly, and  $20 \text{ MeV}/c^2$  for higher masses. The events with  $m(e^+e^-) < 40 \text{ MeV}/c^2$  were not used in the analysis as the acceptance drops very fast in this range.

In Fig. 5, the fitting procedure is illustrated for the first bin,  $m(e^+e^-) = (45 \pm 5) \text{ MeV}/c^2$ , and the case when both the three- and four-cluster events are used. Figure 5(a)

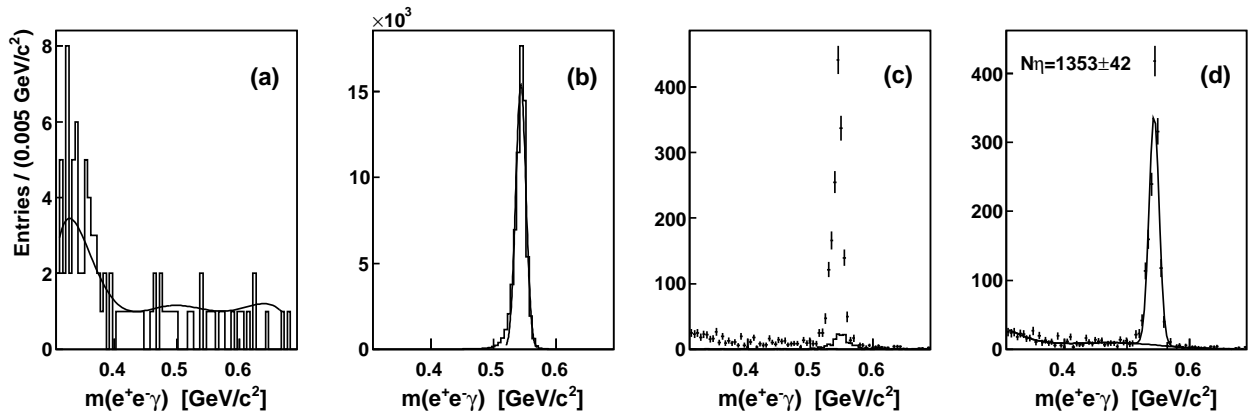


FIG. 6: Same as Fig. 5, but for the four-cluster events only.

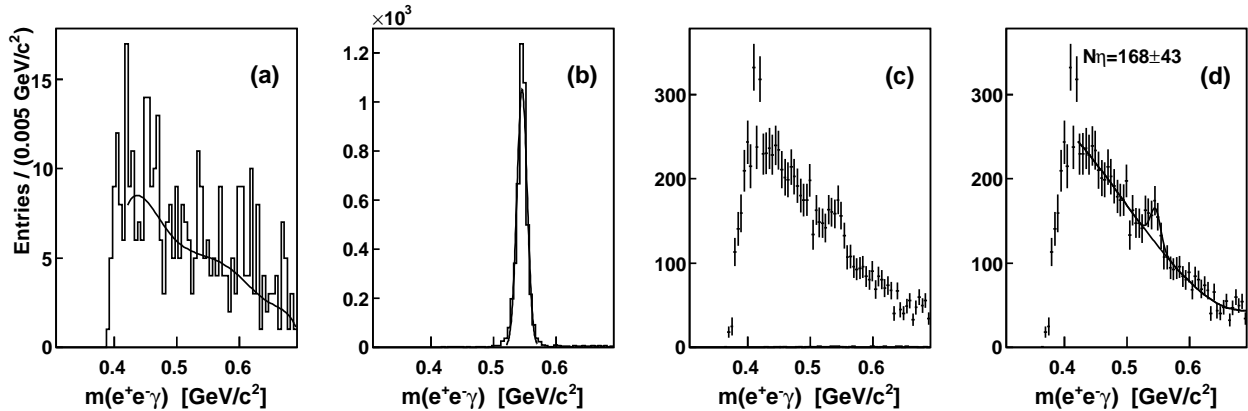


FIG. 7: Same as Fig. 5, but for  $m(e^+e^-) = (370 \pm 10) \text{ MeV}/c^2$ .

depicts the  $m(e^+e^- \gamma)$  invariant-mass distribution for the MC simulation of the background reaction  $\gamma p \rightarrow \pi^0 \pi^0 p$  fitted with a polynomial. Figure 5(b) shows a similar distribution for the MC simulation of  $\gamma p \rightarrow \eta p \rightarrow e^+e^- \gamma p$  fitted with a Gaussian. The experimental distribution after subtracting the random and empty-target background is shown by crosses in Fig. 5(c). The background remaining from  $\gamma p \rightarrow \eta p \rightarrow \gamma \gamma p$  is shown in the same figure by a solid line. Its normalization is based on the number of events generated for  $\gamma p \rightarrow \eta p \rightarrow \gamma \gamma p$  and the number of the  $\gamma p \rightarrow \eta p$  events produced in this experiment. The experimental distribution after subtraction of the  $\gamma p \rightarrow \eta p \rightarrow \gamma \gamma p$  background is shown in Fig. 5(d). A fit to this distribution was done by using the sum of a Gaussian and a polynomial. The mean value and  $\sigma$  of the Gaussian were fixed to the values obtained from the previous fit to the MC simulation for  $\gamma p \rightarrow \eta p \rightarrow e^+e^- \gamma p$ . The initial parameters for the polynomial were taken from the fit to the MC simulation for  $\gamma p \rightarrow \pi^0 \pi^0 p$ .

To provide a good background description in a quite broad range (0.3 – 0.7)  $\text{MeV}/c^2$  of the invariant masses  $m(e^+e^- \gamma)$  for all  $m(e^+e^-)$  bins and selection criteria, an eighth-order polynomial was used for the fits. The order was lowered to six for high  $m(e^+e^- \gamma)$  masses, where

the background range under the  $\eta \rightarrow e^+e^- \gamma$  signal became narrower. It was checked that slight changes of the polynomial order from the used one did not affect the fit results for the  $\eta \rightarrow e^+e^- \gamma$  signal.

The experimental number of  $\eta \rightarrow e^+e^- \gamma$  decays in the  $m(e^+e^- \gamma)$  distribution shown in Fig. 5(d) was determined from the area under the Gaussian. This number,  $1634 \pm 51$  decays, is already greater than the total number of the  $\eta \rightarrow e^+e^- \gamma$  decays,  $1345 \pm 59$ , reported in Ref. [7]. Since the calculation of the experimental number of  $\eta \rightarrow e^+e^- \gamma$  decays was based on the area under a Gaussian, the corresponding detection efficiency was calculated in the same way (i.e., based on a Gaussian fit to the MC simulation for  $\gamma p \rightarrow \eta p \rightarrow e^+e^- \gamma p$ , instead of just using the number of entries in the  $m(e^+e^- \gamma)$  distribution).

The fitting procedure for the same  $m(e^+e^-)$  bin but using only the four-cluster events is illustrated in Fig. 6. Despite a slightly lower peak from the  $\eta \rightarrow e^+e^- \gamma$  signal, a significant improvement of the signal-to-background ratio can be seen.

The fits to both the three- and the four-cluster events were made only up to  $m(e^+e^-) = 400 \text{ MeV}/c^2$ . Above this energy, those fits became unreliable as the signal

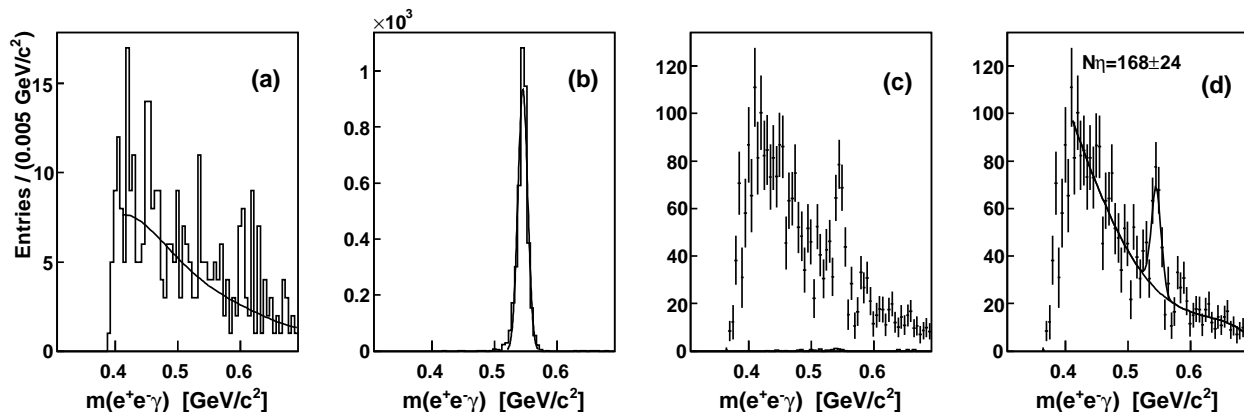


FIG. 8: Same as Fig. 7, but for the four-cluster events only.

from  $\eta \rightarrow e^+e^-\gamma$  decays became comparable with statistical fluctuations of the background. For the four-cluster events, fitting the peak from  $\eta \rightarrow e^+e^-\gamma$  decays was possible up to  $m(e^+e^-) = 460 \text{ MeV}/c^2$ . In Fig. 7, the fitting procedure is illustrated for the range  $m(e^+e^-) = (370 \pm 10) \text{ MeV}/c^2$ , in which a peak from  $\eta \rightarrow e^+e^-\gamma$  decays is still clearly seen for the case when both the three- and the four-cluster events are used. The corresponding fit to only the four-cluster events is shown in Fig. 8. As seen in Figs. 7 and 8, the  $\gamma p \rightarrow \eta p \rightarrow \gamma \gamma p$  background is negligibly small in this range of  $m(e^+e^-)$ , whereas the background under the peak from  $\eta \rightarrow e^+e^-\gamma$  decays increases greatly. Also, the fit yields a sufficiently larger uncertainty in the number of the  $\eta \rightarrow e^+e^-\gamma$  decays for the case of a larger background, i.e., when both the three- and four-cluster events are used.

#### IV. DISCUSSION OF THE RESULTS

The number of the  $\eta \rightarrow e^+e^-\gamma$  decays initially produced in each  $m(e^+e^-)$  bin was obtained by dividing the value from a Gaussian fit to the experimental distribution by the corresponding detection efficiency (see Sec. III for details). Values for  $d\Gamma(\eta \rightarrow e^+e^-\gamma)/dm(e^+e^-)$  were obtained by using the full decay width  $\Gamma_\eta = 1.30 \text{ keV}$  [22] and the total number of  $\eta$  mesons produced, which was determined from an analysis of the process  $\gamma p \rightarrow \eta p \rightarrow 3\pi^0 p$  in the same data set [19] and using 0.3257 for the  $\eta \rightarrow 3\pi^0$  branching ratio [22]. The results for  $d\Gamma(\eta \rightarrow e^+e^-\gamma)/dm(e^+e^-)$  obtained by using only the four-cluster events are shown by solid squares in Fig. 9(a). The corresponding results obtained for the sum of the three- and four-cluster events are shown in the same figure by open circles. As seen, in the range of the latter results,  $m(e^+e^-) < 400 \text{ MeV}/c^2$ , the  $d\Gamma(\eta \rightarrow e^+e^-\gamma)/dm(e^+e^-)$  values of both the approaches are in good agreement within their error bars. The QED prediction for  $d\Gamma(\eta \rightarrow l^+l^-\gamma)/dm(l^+l^-)$  with  $|F_\eta|^2 = 1$  is depicted in Fig. 9(a) by a dashed line, and the QED prediction including the  $\eta$  TFF with  $\Lambda^{-2} = 1.95 \text{ GeV}^{-2}$

(most precise experimental result from the NA60 [8, 9]) is shown by a solid line. One can see that the results of this work are much closer to the prediction based on the NA60 data.

The results for the  $\eta$  TFF,  $|F_\eta|^2$ , were obtained by dividing the  $d\Gamma(\eta \rightarrow e^+e^-\gamma)/dm(e^+e^-)$  values by the QED term of Eq. (1) and using 0.3931 for the  $\eta \rightarrow \gamma\gamma$  branching ratio [22]. In Fig. 9(b), the  $|F_\eta(m_{ll})|^2$  values are shown by solid squares for the case of using only the four-cluster events and by open circles for all events. As seen, the TFF results of both the approaches are in good agreement within their error bars. Because of the background under the  $\eta \rightarrow e^+e^-\gamma$  signal, the uncertainties of the data points do not reflect the actual statistic for the  $\eta \rightarrow e^+e^-\gamma$  decays observed, which was  $1.8 \cdot 10^4$  and  $2.2 \cdot 10^4$  for only four-cluster and all events, respectively. Some staggering of the data points is also caused by statistical fluctuations of background events under the  $\eta \rightarrow e^+e^-\gamma$  peak.

Since the data based only on the four-cluster events have a better signal-to-background ratio, resulting in smaller fit uncertainties, and a wider covering of the  $m(e^+e^-)$  range, they are considered as the main results of this work. Their numerical values are listed in Table I. The magnitude of  $\Lambda^{-2}$  was obtained by fitting the  $\eta$  TFF parametrized as defined in Eq. (2) to the main  $|F_\eta|^2$  results. As discussed in the Introduction, the fit was made with two free parameters, one of which,  $p_1$ , is  $\Lambda^{-2}$  itself, and the other,  $p_0$ , reflects the general normalization of the data points, which could be different from  $p_0 = 1$  because of the uncertainty in the determination of the experimental number of  $\eta$  mesons produced. The correlation between the two parameters results in a larger fit error for  $\Lambda^{-2}$ . However, this fit error already includes the systematic uncertainty in the general normalization of the data points.

The two-parameter fit to the main  $|F_\eta|^2$  data points is shown in Fig. 9(b) by a solid line. This fit yields the values  $p_0 = 0.982 \pm 0.011$  for the normalization parameter and  $p_1 = (1.95 \pm 0.15) \text{ GeV}^{-2}$  for  $\Lambda^{-2}$ . For simplicity, the fit error for  $\Lambda^{-2}$  will be called its statistical uncertainty



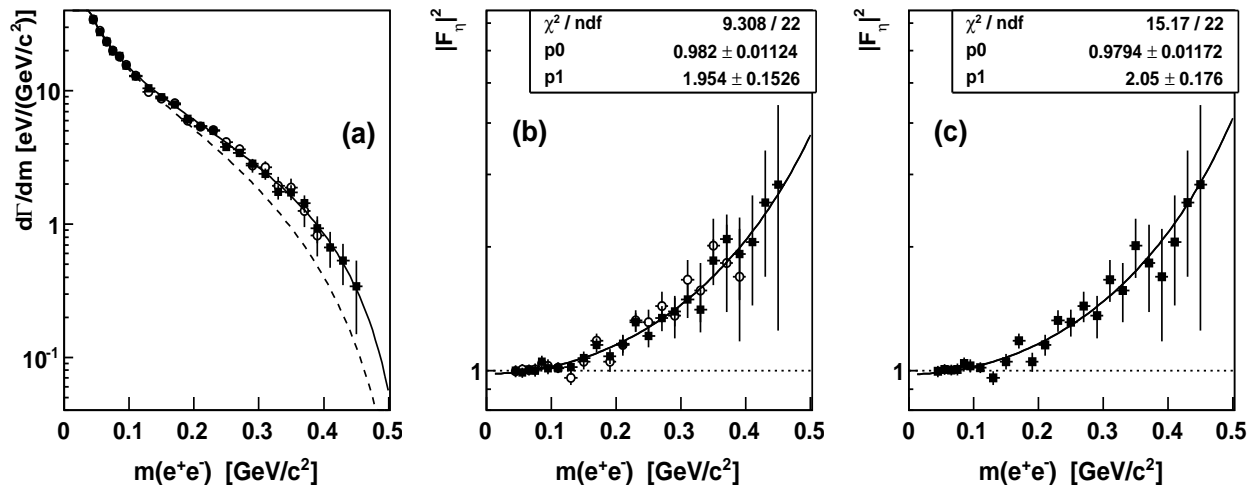


FIG. 9: (a) Results for  $d\Gamma(\eta \rightarrow e^+e^-\gamma)/dm(e^+e^-)$  obtained by using the four-cluster events only (solid squares) and both the three- and the four-cluster events (open circles). The QED prediction with  $|F_\eta|^2 = 1$  and the QED prediction including the  $\eta$  TFF with  $\Lambda^{-2} = 1.95 \text{ GeV}^{-2}$  are shown by a dashed and a solid line, respectively. (b) Main results (based on the four-cluster events only) of this work (solid squares) for  $|F_\eta(m_{e^+e^-})|^2$  compared to the results based on all events (open circles); the solid line shows a fit of the  $\eta$  TFF parametrized as Eq. (2) to the main results. (c) Fit (solid line) to results for  $|F_\eta(m_{e^+e^-})|^2$  obtained from combining the three- and four-cluster events, and used then to estimate the systematic uncertainty in the  $\Lambda^{-2}$  value.

TABLE I: Results of this experiment for the  $\eta$  TFF,  $|F_\eta|^2$ , as a function of the invariant mass  $m(e^+e^-)$

$m(e^+e^-)$ [MeV/ $c^2$ ]	$45 \pm 5$	$55 \pm 5$	$65 \pm 5$	$75 \pm 5$	$85 \pm 5$	$95 \pm 5$
$ F_\eta ^2$	$0.999 \pm 0.031$	$0.988 \pm 0.029$	$1.005 \pm 0.030$	$0.999 \pm 0.031$	$1.051 \pm 0.034$	$1.014 \pm 0.036$
$m(e^+e^-)$ [MeV/ $c^2$ ]	$110 \pm 10$	$130 \pm 10$	$150 \pm 10$	$170 \pm 10$	$190 \pm 10$	$210 \pm 10$
$ F_\eta ^2$	$1.014 \pm 0.028$	$1.019 \pm 0.037$	$1.071 \pm 0.041$	$1.153 \pm 0.044$	$1.083 \pm 0.046$	$1.161 \pm 0.056$
$m(e^+e^-)$ [MeV/ $c^2$ ]	$230 \pm 10$	$250 \pm 10$	$270 \pm 10$	$290 \pm 10$	$310 \pm 10$	$330 \pm 10$
$ F_\eta ^2$	$1.312 \pm 0.068$	$1.214 \pm 0.076$	$1.342 \pm 0.094$	$1.393 \pm 0.113$	$1.487 \pm 0.144$	$1.406 \pm 0.170$
$m(e^+e^-)$ [MeV/ $c^2$ ]	$350 \pm 10$	$370 \pm 10$	$390 \pm 10$	$410 \pm 10$	$430 \pm 10$	$450 \pm 10$
$ F_\eta ^2$	$1.851 \pm 0.235$	$2.086 \pm 0.306$	$1.918 \pm 0.433$	$2.05 \pm 0.61$	$2.56 \pm 0.87$	$2.83 \pm 1.58$

throughout the rest of this paper.

The results based on the sum of the three- and four-cluster events were used to estimate the systematic uncertainty that comes from fitting the background under the  $\eta \rightarrow e^+e^-\gamma$  peak (as the two subsets have different levels of background) and from the acceptance correction, including the detection efficiency for the outgoing proton. This systematic uncertainty was estimated by replacing the main  $|F_\eta|^2$  results below  $m(e^+e^-) = 400 \text{ MeV}/c^2$  with the results obtained from the sum of the three- and four-cluster events and repeating the fit with the  $\eta$  TFF parametrized as Eq. (2). This fit, demonstrated in Fig. 9(c), yields  $\Lambda^{-2} = (2.05 \pm 0.18) \text{ GeV}^{-2}$ , which, within the uncertainties, is in good agreement with the value obtained from the fit to the main results. The difference between the two results was taken as the systematic uncertainty in the value of  $\Lambda^{-2}$  measured in this work. Then, the final value for the present measurement

is

$$\Lambda^{-2} = (1.95 \pm 0.15_{\text{stat}} \pm 0.10_{\text{syst}}) \text{ GeV}^{-2}, \quad (3)$$

which is in very good agreement within the errors with all recent results reported in Refs. [7–9]. As seen in Fig. 10, the  $|F_\eta(m_{ll})|^2$  results of this work are in similar good agreement within the error bars with the data points from Refs. [7, 8].

The uncertainty reached for the  $\Lambda^{-2}$  value in the present work is smaller than those of all previous measurements based on the  $\eta \rightarrow e^+e^-\gamma$  decay, is of a similar magnitude as the NA60 value from peripheral In–In data [8], and still yields to the latest, preliminary result of the NA60 from  $p-A$  collisions [9].

In Fig. 10, the results of this work for  $|F_\eta(m_{ll})|^2$  are also compared to three different theoretical predictions. Since all models assume that  $|F_\eta(m_{ll} = 0)|^2 = 1$ , for a better comparison, the fit to the data points from

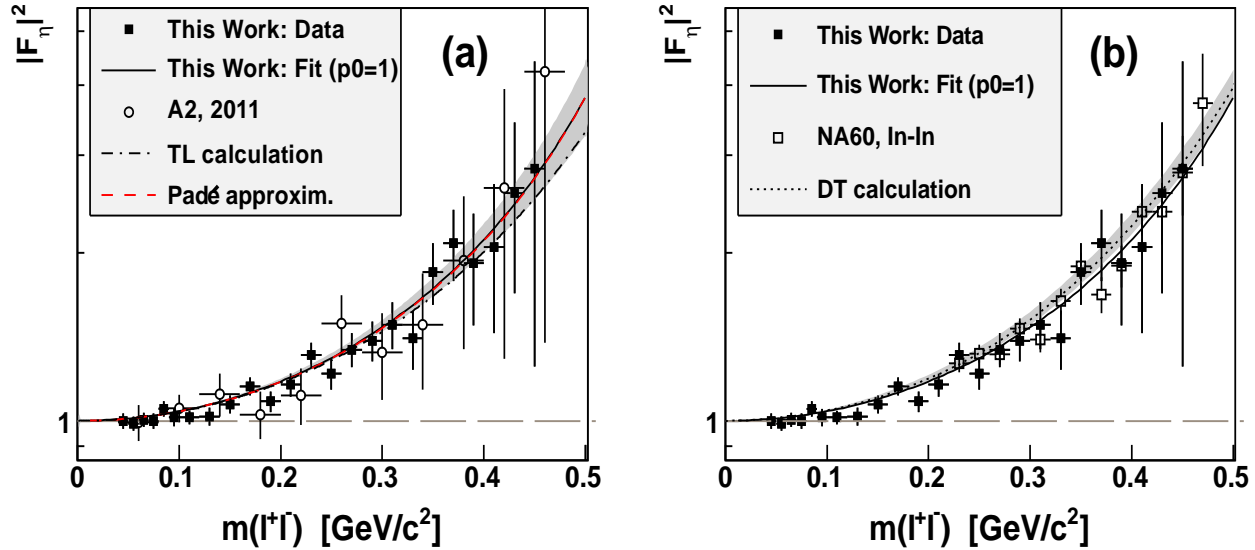


FIG. 10: (Color online) Results of this work (solid squares) for the  $\eta$  TFF,  $|F_\eta(m_{ll})|^2$ , compared to other recent measurements and theoretical predictions: former data of the A2 Collaboration [7] (open circles in (a)) and the NA60 in peripheral In–In data [8] (open squares in (b)), calculations of Ref. [25] (dash-dotted line in (a)), Ref. [28] (red dashed line with an error band in (a)), and Ref. [32] (dotted line with an error band in (b)). The solid line is the fit from Fig. 9(b) rescaled so that  $p_0 = 1$ .

Fig. 9(b) is rescaled by setting its normalization parameter to  $p_0 = 1$  and leaving its second parameter  $p_1$ , reflecting the slope parameter  $\Lambda^{-2}$ , unchanged. The calculation by Terschlüsen and Leupold (TL) combines the vector-meson Lagrangian proposed in Ref. [23] and recently extended in Ref. [24], with the Wess-Zumino-Witten contact interaction [25] (see also Ref. [26] for the corresponding case of the  $\pi^0$  TFF). Their calculation agrees very well with the standard VMD form factor. As seen, the TL calculation (shown in Fig. 10(a) by a dash-dotted line) goes slightly lower than the pole-approximation (Eq. (2)) fit to the present data, whereas it fully describes the data points within the error bars.

The second calculation is based on a model-independent method using Padé approximants that was developed for the  $\pi^0$  TFF in Ref. [27]. Using spacelike data (CELLO [29], CLEO [30], BABAR [31]), this method provides a parametrization that is also suited to describe data in the  $m_{ll}$  range from zero to  $\sqrt{0.4}$  GeV/ $c^2$ , and thus provides a model-independent prediction for the timelike TFF [28]. Over the full  $m_{ll}$  range, this calculation (shown in Fig. 10(a) by a red dashed line with an error band) practically overlaps with the pole-approximation fit to the present data points.

In another recent calculation [32] by the Jülich group, the connection between the radiative decay  $\eta \rightarrow \pi^+\pi^-\gamma$  and the isovector contributions of the  $\eta \rightarrow \gamma\gamma^*$  TFF is exploited in a model-independent way, using dispersion theory (DT). This calculation (shown in Fig. 10(b) by a dotted line with an error band) goes slightly above the fit to the present data.

Currently, the VMD models that are used to calculate

the contribution of the hadronic light-by-light scattering to  $(g-2)_\mu$  include only  $\rho$ ,  $\omega$ , and  $\phi$  resonances. These contributions are calculated with  $\Lambda = (774 \pm 29)$  MeV close to the  $\rho$ -meson mass. This value of  $\Lambda$  was determined from a fit to spacelike data measured by the CLEO collaboration [30] down to the momentum transfer  $q^2 = -1.5$  GeV $^2$ , which is far away from  $q^2 = 0$  GeV $^2$ . The  $\Lambda$  value from CLEO disagrees with the VMD value,  $\Lambda = 745$  MeV. It also disagrees with the result of this work,  $\Lambda = (716 \pm 0.033)$  MeV, by more than one standard deviation, where both the measurements are of a similar accuracy. However, the measurement presented in this work was performed much closer to  $q^2 = 0$  GeV $^2$ , and it agrees very well with earlier measurements of the  $\eta \rightarrow e^+e^-\gamma$  Dalitz decay, just improving their accuracy. Though the results of this work are not able to rule out the VMD models used for calculating  $(g-2)_\mu$ , one can see that smaller values for  $\Lambda$  should be used in those calculations, indicating that contributions from heavier vector-meson resonances, like, e.g.,  $\rho'$ , might not be completely negligible.

## V. SUMMARY AND CONCLUSIONS

A new determination of the electromagnetic transition form factor from the  $\eta \rightarrow e^+e^-\gamma$  Dalitz decay was presented in this paper. The statistical accuracy achieved in this work surpasses all previous measurements of  $\eta \rightarrow e^+e^-\gamma$  and matches the NA60 result based on  $\eta \rightarrow \mu^+\mu^-\gamma$  decays from peripheral In–In collisions. Compared to the former determination of the  $\eta$  TFF by

the A2 Collaboration, an increase by more than one order of magnitude in statistic has been achieved. This was accomplished by an analysis of three times more data and the use of a kinematic-fit technique, which allowed for far looser cuts and for exploiting the full  $\eta$  production range available at MAMI-C. The extracted slope parameter  $\Lambda^{-2} = (1.95 \pm 0.15_{\text{stat}} \pm 0.10_{\text{syst}}) \text{ GeV}^{-2}$  agrees within the uncertainties with the results from all recent measurements of the  $\eta$  TFF. A pole-approximation fit to the presented data shows almost perfect agreement with the model-independent calculation from Ref. [28]. The calculation by Terschlüsen and Leupold [25] and the DT calculation [32] deviate slightly from the fit, but the statistical uncertainties are still not sufficient to rule out any of the theoretical predictions. Thus, a need for more precise measurements is evident, though the results of this work indicate clearly that smaller effective vector-meson masses  $\Lambda$  should be used in VMD-like models for calculating the contribution of the hadronic light-by-light scattering to  $(g-2)_{\mu}$ , as well as rare  $\eta$  decays and all processes involving the  $\eta$  TFF.

### Acknowledgment

The authors wish to acknowledge the excellent support of the accelerator group and operators of MAMI.

We would like to thank Pablo Sanchez-Puertas for many fruitful discussions. This work was supported by the Deutsche Forschungsgemeinschaft (SFB443, SFB/TR16, and SFB1044), DFG-RFBR (Grant No. 09-02-91330), the European Community-Research Infrastructure Activity under the FP6 “Structuring the European Research Area” program (Hadron Physics, Contract No. RII3-CT-2004-506078), Schweizerischer Nationalfonds, the U.K. Science and Technology Facilities Council, the U.S. Department of Energy and National Science Foundation, INFN (Italy), and NSERC (Canada). The work of P. Masjuan was supported by the Cluster of excellence “PRISMA” of the Deutsche Forschungsgemeinschaft and the State of Rhineland Palatinate, Germany. A. Fix acknowledges additional support from the Russian Federation federal program “Kadry” (Contract No. P691) and the MSE Program “Nauka” (Contract No. 1.604.2011). We thank the undergraduate students of Mount Allison University and The George Washington University for their assistance.

- 
- [1] E. Czerwinski, S. Eidelman, C. Hanhart, B. Kubis, A. Kupść, S. Leupold, P. Moskal, and S. Schadmand (Editors), *Proceedings of First MesonNet Workshop on Meson Transition Form Factors*, 2012, Cracow, Poland, arXiv:1207.6556 [hep-ph].
- [2] L.G. Landsberg, *Phys. Rep.* **128**, 301 (1985).
- [3] J.J. Sakurai, *Currents and mesons*, University of Chicago Press, Chicago, USA, 1969.
- [4] R. Escribano and J.M. Frere, *J. High En. Phys.* **0506**, 029 (2005).
- [5] R. Escribano and J. Nadal, *J. High En. Phys.* **0705**, 006 (2007).
- [6] F. Jegerlehner and A. Nyffeler, *Phys. Rep.* **477**, 1 (2009).
- [7] H. Berghäuser *et al.*, *Phys. Lett. B* **701**, 562 (2011).
- [8] R. Araldi *et al.*, *Phys. Lett. B* **677**, 260 (2009).
- [9] A. Uras for the NA60 Collaboration, *Acta Phys. Pol. B* **5**, 465 (2012).
- [10] A. Starostin *et al.*, *Phys. Rev. C* **64**, 055205 (2001).
- [11] R. Novotny, *IEEE Trans. Nucl. Sci.* **38**, 379 (1991).
- [12] A.R. Gabler *et al.*, *Nucl. Instr. Meth. A* **346**, 168 (1994).
- [13] H. Herminghaus *et al.*, *IEEE Trans. Nucl. Sci.* **30**, 3274 (1983).
- [14] K.-H. Kaiser *et al.*, *Nucl. Instr. Meth. A* **593**, 159 (2008).
- [15] J.C. McGeorge *et al.*, *Eur. Phys. J. A* **37**, 129 (2008).
- [16] I. Anthony *et al.*, *Nucl. Instr. Meth. A* **310**, 230 (1991).
- [17] S.J. Hall *et al.*, *Nucl. Instr. Meth. A* **368**, 698 (1996).
- [18] S. Prakhov *et al.*, *Phys. Rev. C* **79**, 035204 (2009).
- [19] E.F. McNicoll *et al.*, *Phys. Rev. C* **82**, 035208 (2010).
- [20] D. Watts, *Proceedings of the 11th International Conference on Calorimetry in Particle Physics*, Perugia, Italy, 2004 (World Scientific, 2005) p. 560.
- [21] V.L. Kashevarov *et al.*, *Phys. Rev. C* **85**, 064610 (2012).
- [22] J. Beringer *et al.* (Particle Data Group), *Phys. Rev. D* **86**, 010001 (2012).
- [23] M.F.M. Lutz and S. Leupold, *Nucl. Phys. A* **813**, 96 (2008).
- [24] C. Terschlüsen, S. Leupold, and M.F.M. Lutz, *Eur. Phys. J. A* **48**, 190 (2012).
- [25] C. Terschlüsen, Diploma Thesis, University of Gießen, 2010.
- [26] C. Terschlüsen and S. Leupold, University of Uppsala, private communication, 2013.
- [27] C. Terschlüsen, B. Strandberg, S. Leupold, and F. Eichstädt, *Eur. Phys. J. A* **49**, 116 (2013).
- [28] P. Masjuan, *Phys. Rev. D* **86**, 094021 (2012).
- [29] R. Escribano, P. Masjuan, and P. Sanchez-Puertas, *Phys. Rev. D* **89**, 034014 (2014).
- [30] H.J. Behrend *et al.*, *Z. Phys. C* **49**, 401 (1991).
- [31] J. Gronberg *et al.*, *Phys. Rev. D* **57**, 33 (1998).
- [32] P. del Amo Sanchez *et al.*, *Phys. Rev. D* **84**, 052001 (2011).
- [33] C. Hanhart, A. Kupść, U.-G. Meißner, F. Stollenwerk, and A. Wirzba, *Eur. Phys. J. C* **73**, 2668 (2013); C. Hanhart, Forschungszentrum Jülich, private communication, 2013.